

0.1 Drag force experiments

As we introduced in the last section of **Experimental approach** chapter, we used the full frequency sweep method for vibrating wire and tuning fork. Each point on following graphs was obtained by a pair of full frequency sweeps across the resonance of given oscillator. One sweep was performed with increasing frequency and the second one with decreasing frequency, which made us confident that no hysteresis effect was present.

We present all the measurements in the form of typical hydrodynamic visualizations (velocity-force response, drag coefficients and appropriate dimensionless numbers) of oscillating wire, torsional disc and tuning fork, respectively.

0.1.1 Vibrating wire

We were measuring the voltage in phase with the driving current to obtain the resonant response. Above high enough applied drives (~ 0.8 mA at temperature 1.67 K responding in ~ 0.1 m/s peak velocity), there was present a frequency shift and a *peak softening* effect. Together with a poor calibration of magnetic field produced by permanent magnets, the peak velocity on the wire top is known with the accuracy about $\pm 20\%$. Fortunately, this error doesn't affect the scaling process.

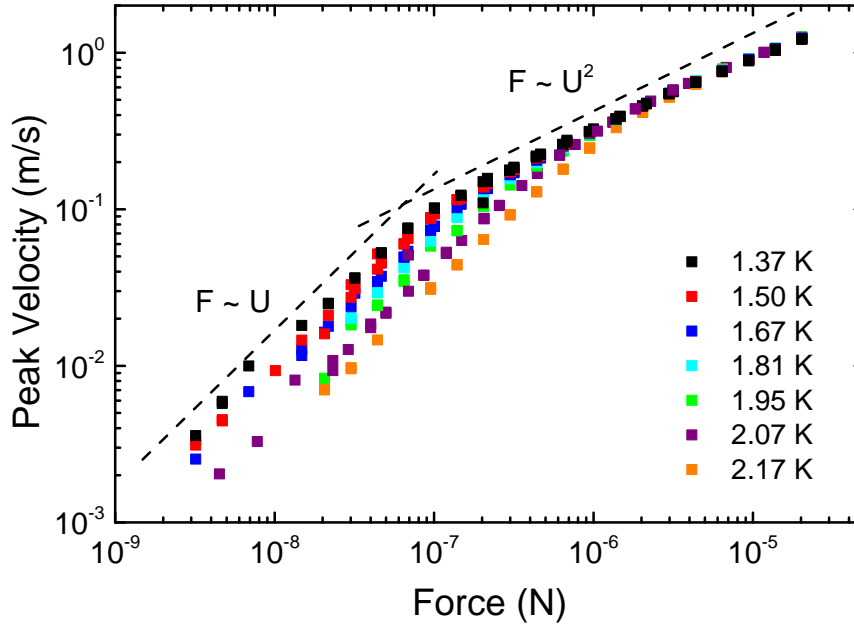


Figure 1: Plot of peak velocity U_0 against the applied peak force F_0 for the vibrating wire submerged in superfluid ^4He at several temperatures. The black dashed lines serve as sketch of theoretical laminar and turbulent regimes.

We plotted in **Figure (1)** the peak velocity of the wire top U_0 against the applied peak force F_0 at various temperatures from two-fluid regime ($T > 1.0$ K).

Clearly, the wire exhibits linear drag at low velocities and non-linear additional drag in the area of higher velocities. The energy losses of the wire in the low-velocity part are dominated by the viscous drag of the present normal component. Other loss mechanisms like acoustic emission are in principle present as well, but neglected in further discussion. The additional dissipation process in the higher-velocity part indicates either classical or quantum turbulence (or both) and the measured drag F_0 is roughly proportional to U_0^2 .

Next we plotted in **Figure (2)** the classical drag coefficient as a function of peak force and velocity $C_D \sim F_0/U_0^2$ using the same data as presented in **Figure (1)**.

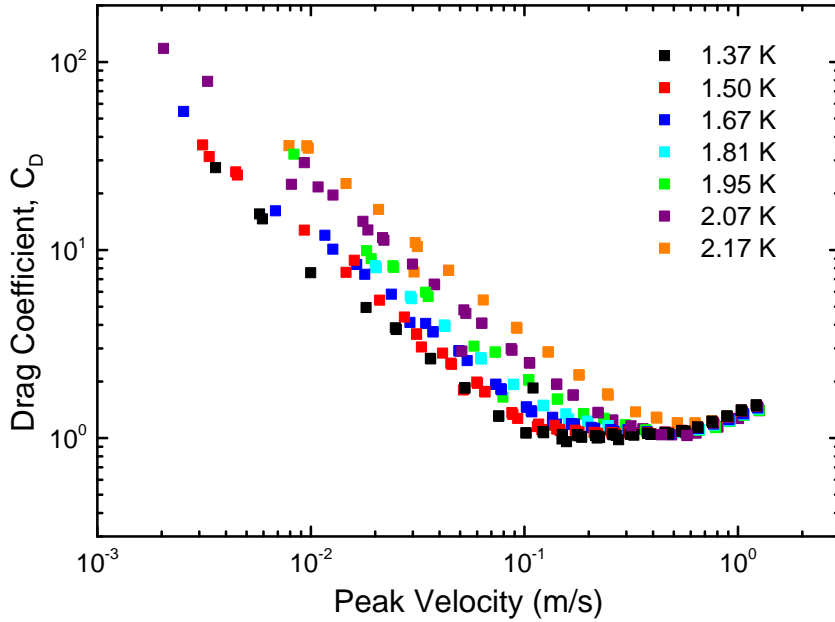


Figure 2: Plot of drag coefficient C_D against the velocity peak response U_0 for the vibrating wire at several temperatures.

In order to perform the universal scaling, we collapse the contribution of the normal component in the following way:

$$C_D^n \leftarrow C_D \frac{\rho}{\rho_n}, \quad \text{Dn} \leftarrow U_0 \sqrt{\frac{2\rho_n}{\eta\omega}}, \quad (1)$$

where η is the dynamical viscosity of Helium-II for a given temperature. Relations in (1) are applied in the same way as described (??), (??) in the last section of **Theoretical background** chapter.

The resulting plot **Figure (3)** clearly collapses all the linear parts of the measured

drag. However, the theoretical pre-factor ($\Phi_{\text{cyl}} = 4\pi$) is smaller than the fitted one ($\Phi \sim 26$). This is most likely caused by the irregularities on the surface of the wire. Indeed, excrescences of order $5\mu\text{m}$ were observed on the $40\mu\text{m}$ wire under an optical microscope.

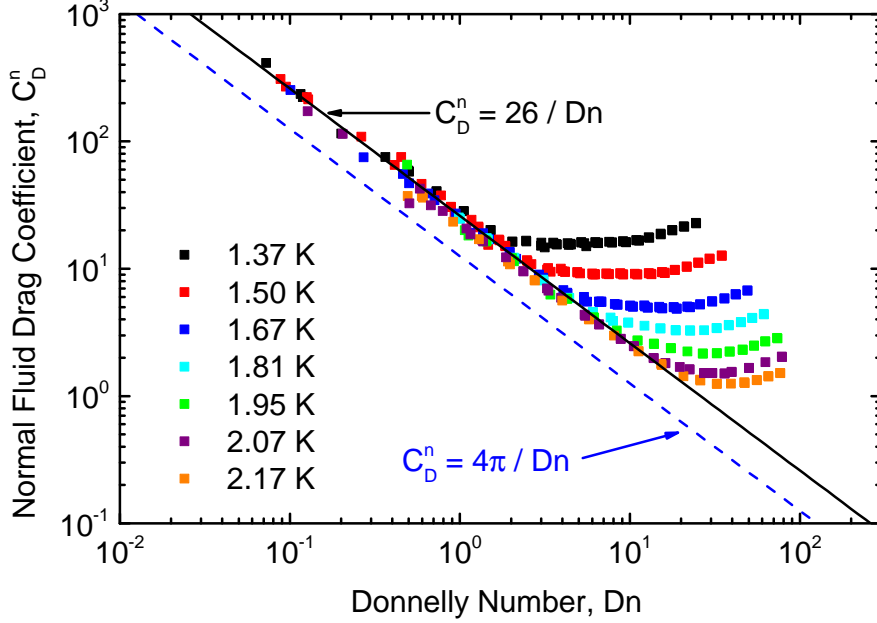


Figure 3: Plot of normal fluid drag coefficient C_D^n against the dimensionless Donnelly number (Dn) for the vibrating wire at several temperatures. The blue dashed line shows the expected theoretical dependence [?] for a smooth cylinder. The solid black line is a numerical fit of the linear part of data.

One may see from the **Figure (3)** that all temperature curves are visually sorted ascendingly as the non-linear behaviour occurs at some starting points. This is clear sign the Donnelly number cannot govern the turbulent process and thus it is a clear sign of the onset of quantum turbulence by the superfluid component.

0.1.2 Oscillating disc

The (torsionally) oscillating disc differs from the vibrating wire in several technicalities:

- Oscillating disc does not displace any fluid and thus The superfluid is at rest unless quantized vorticity is produced
- It is not possible to perform measurements in a steady state of flow, but decayed flow was measured instead
- Drag force has to be inferred from the decaying amplitude of oscillator deflection.

As a consequence of mentioned differences (examples showed in **Figure 4**), we have to substitute $U_0 = \omega R \phi_0$ within the Donnelly number and define a new drag coefficient, specific for our mechanical system of torsionally oscillating disc in a viscous fluid of density ρ_n as:

$$C_D^n \leftarrow \frac{2M_f}{A\rho_n\Omega_0^2 R^3}, \quad \text{Dn} \leftarrow R\omega\phi_0\sqrt{\frac{2\rho_n}{\eta\omega}}, \quad (2)$$

where M_f is the moment of friction forces, R the radius of the disc, $A = \pi R^2$ the area of the disc and Ω_0 is the amplitude of angular frequency $\omega(t)$. It was already showed [?] the relation between such drag coefficient (2) can be expressed in laminar flow in terms of the Donnelly number as $C_D^n = \Phi/\text{Dn}$ with the pre-factor $\Phi_{\text{disc}} = 2$.

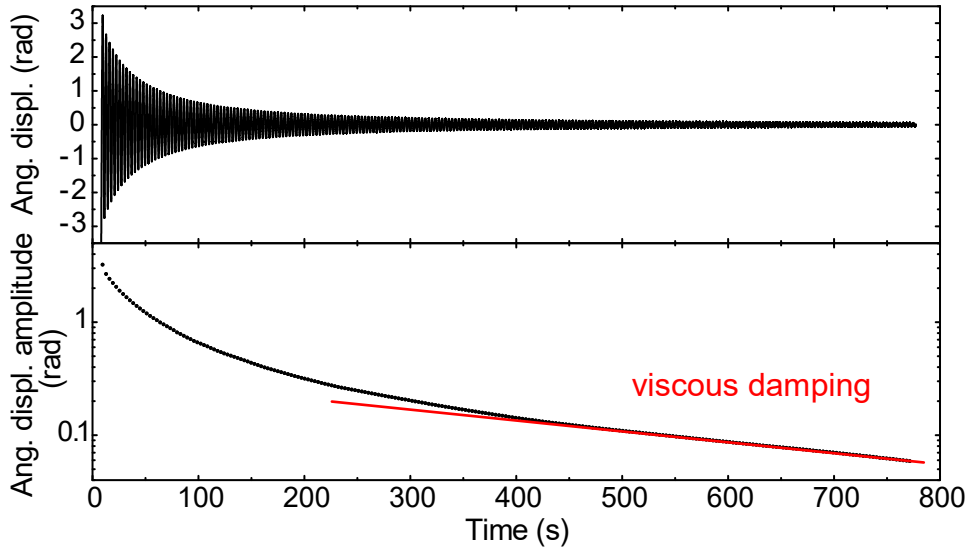


Figure 4: Example of angular displacement measurement in time of the torsionally oscillating disc. Top picture: The decreasing angular displacement amplitudes $\phi_0(t)$. Bottom picture: The logarithmic plot $\phi_0(t)$ shows two distinct regions – nonlinear decay in the area of earlier times $t < 400$ due to turbulent drag forces and an exponential (viscous) decay due to laminar flow of the normal component at the later times $t > 500$.

We plot the re-defined drag coefficient (2) against the Donnelly number in **Figure 5**.

Again, as in case of vibratig wire, in the area of small values of Donnelly number, the data clearly collapse to a single dependence, which illustrates the universal scaling idea. One would naturally expect the normal component to transit to turbulent regime earlier than the superfluid one since the oscillating disc directly moves only with the normal component. However, **Figure 5** clearly shows that non-linearities are not characterized by a single value of Dn , but rather continuously with ascending temperature. This implies that instabilities cannot be explained by pure viscous fluid dynamics and must relate to

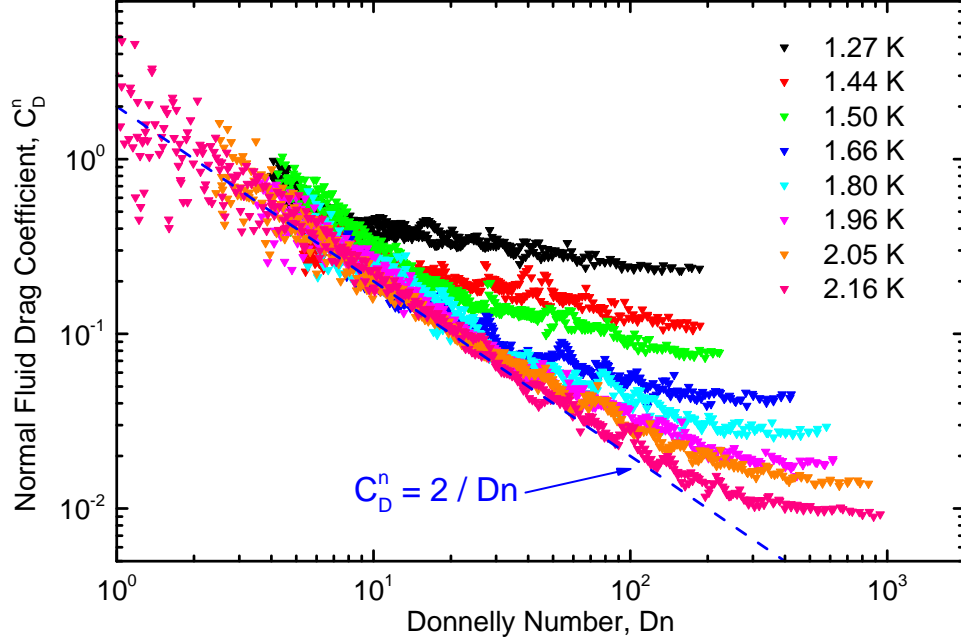


Figure 5: Plot of re-defined fluid drag coefficient C_D^n against the dimensionless Donnelly number (Dn) for the torsionally oscillating disc at several temperatures. The blue dashed line shows the expected theoretical dependence [?] for viscous drag. The temperature-dependent and temperature-ascending starting points of non-linearities are a clear sign of the onset of quantum turbulence by the superfluid component.

the quantum turbulence of vortex tangle.

0.1.3 Tuning fork

As the last oscillator, we used quartz tuning fork with geometry and resonant specifics as they were described in **Experimental approach** chapter. the resonant response was experimentally measured in the same way as was with vibrating wire - by a real-time analysis of in-phase current response. Electrical quantities are then converted into physical attributes according to mentioned relations ??, which are dependent on fork constants $a_{f0} = 3.665 \times 10^{-7} \text{ Cm}^{-1}$, $a_{f1} = 14.094 \times 10^{-7} \text{ Cm}^{-1}$ for the fundamental and overtone mode, respectively.

In order to measure the fork constants, we had to perform a series of frequency sweeps in low-temperature vacuum. We estimate the uncertainty of fork constants to be of 10% since velocity calculation errors were proven using optical experiments.

In **Figure 6** we plot the peak velocity response U_0 of the top of the fork prong, against the applied peak force F_0 at various temperatures from two-fluid regime ($T > 1.0$ K). We sketched the theoretical laminar and classical turbulent dependences as guides for the eye.

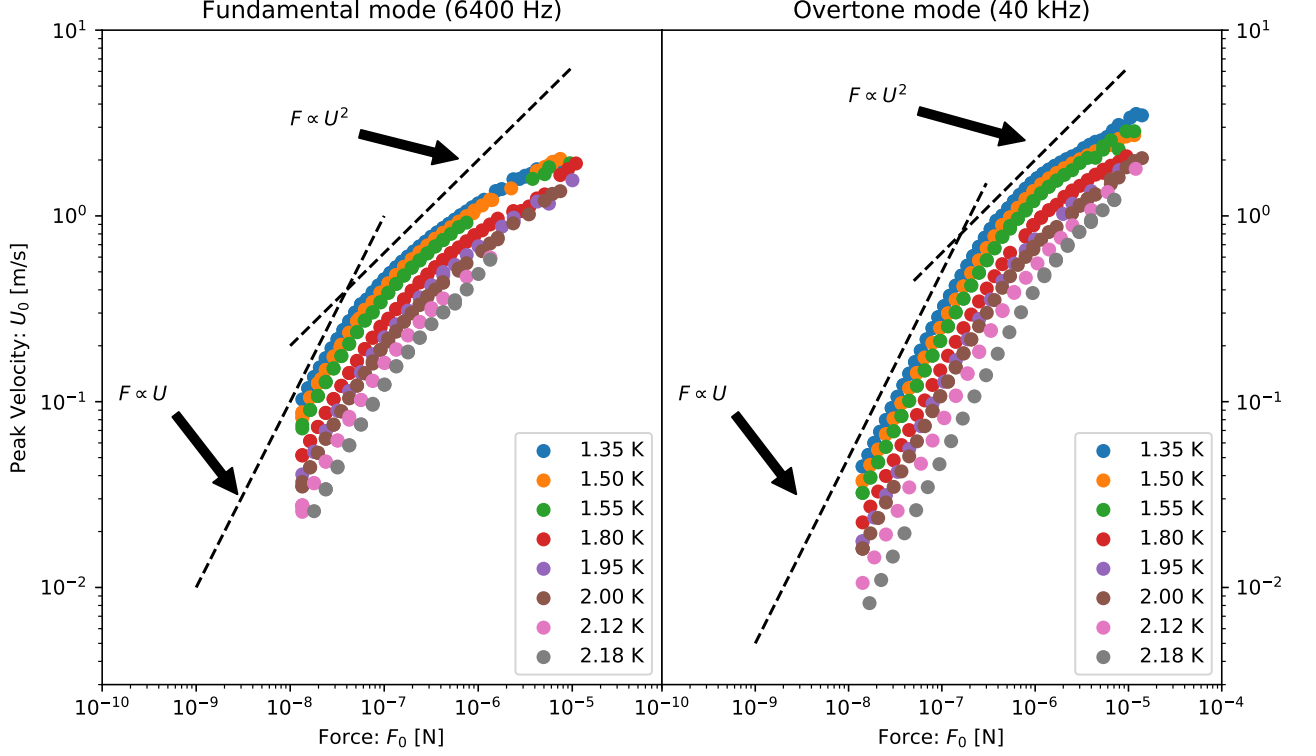


Figure 6: Plot of peak velocity U_0 against the applied peak force F_0 for the oscillating tuning fork submerged in superfluid ^4He at several temperatures.

Left image: Measurements in fork's fundamental mode, Right image: Measurements in fork's overtone mode, Black dashed lines: Sketch of theoretical laminar and classical turbulent regime dependencies.

Next, we plot in **Figure 7** the classical drag coefficient C_D against the peak velocity U_0 . Both oscillating modes are visualised as a paired plot in order to show their shared asymptote (as sketched with the black dashed line) in the area of big velocities. Also, we sketched the laminar regime fit as a demonstration.

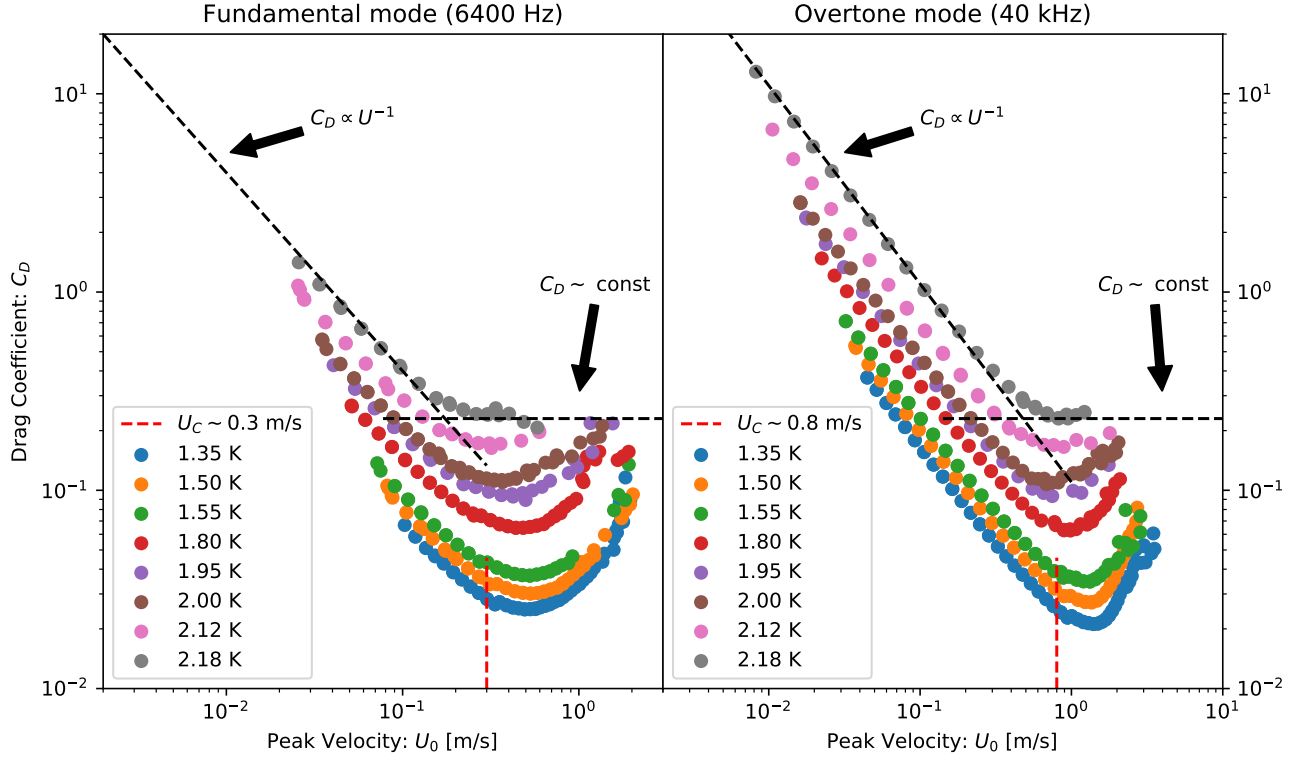


Figure 7: Plot of drag coefficient C_D against the velocity peak response U_0 for the oscillating tuning fork submerged in superfluid ^4He at several temperatures.

Left image: Measurements in fork's fundamental mode, Right image: Measurements in fork's overtone mode, Black dashed lines: Sketch of theoretical laminar and classical turbulent regime dependencies, Red dashed line: Critical value of velocity U_C above which an onset of quantum turbulence appears. The clear sign of this effect can be seen for a group of curves with $T < 1.6$ K.

As expected, the tuning fork exhibits a linear drag in the area of low velocities regardless on the temperature from the studied range. Then, approximately above the critical velocity U_C , a synchronized increased drag was observed for a group of curves with temperature $T < 1.6$ K, which is a clear sign of onset of quantum turbulence. The critical velocities differ for oscillating modes:

$$U_{C0} \sim 0.3 \text{ m/s} \quad U_{C1} \sim 0.8 \text{ m/s}, \quad (3)$$

which is expected from the scaling relation (??) and roughly proven since the critical dimensionless velocities $\hat{U}_{C0} = U_{C0}/\sqrt{\kappa\omega_0} \approx 4.7$ and $\hat{U}_{C1} = U_{C1}/\sqrt{\kappa\omega_1} \approx 5.0$ are similar.

Curves with higher temperature seem to transit to non-linear regime earlier, which indicates the classical turbulence of the normal component instead.

To characterize the normal component flow, we plot in **Figure 8** the normal drag coefficient against the dimensionless Donnelly number. The conversions were done as we stated in (1).

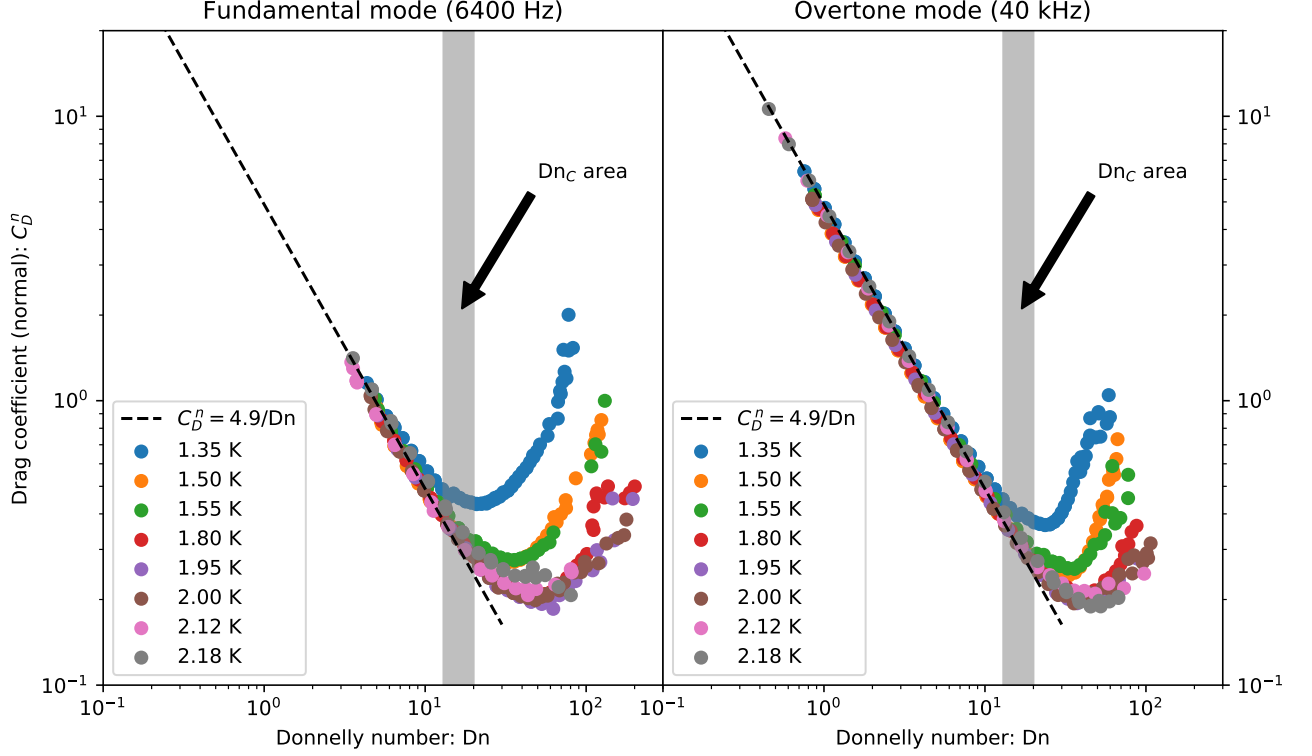


Figure 8: Normal fluid drag coefficient C_D^n as a function of the Donnelly number Dn . Left image: Measurements in fork's fundamental mode, Right image: Measurements in fork's overtone mode, Black dashed line: the laminar drag, fitted with the same pre-factor $C_D^n = 4.9/Dn$ for both oscillation modes, Grey area: the possible critical values for Dn , above which the onset of classical turbulence occurs for the curves with temperature $T > 1.6$ K.

With no doubt, in the area of low Donnelly values, the dependencies collapse to a single dependence as expected, representing the laminar regime with the shared pre-factor $\Phi \sim 4.9$. In contrast to the results obtained with the vibrating wire or oscillating disc, we recognize a critical value of Donnelly number Dn_{crit} above which the rest group of temperature curves $T > 1.6$ K non-linearly deviate. The onset of turbulence is governed by a single value of Donnelly number Dn_C and thus dominated by the normal component of Helium-II.

In order to find at least an approximate value for the shared critical value of Donnelly number, we also plot in **Figure (9)** the numerical errors from a fitted laminar dependence: $C_D^n \text{Dn} - \Phi$, where $\Phi = 4.9$, against the Donnelly number to see more clearly when the group of temperatures $T > 1.6$ K deviates.

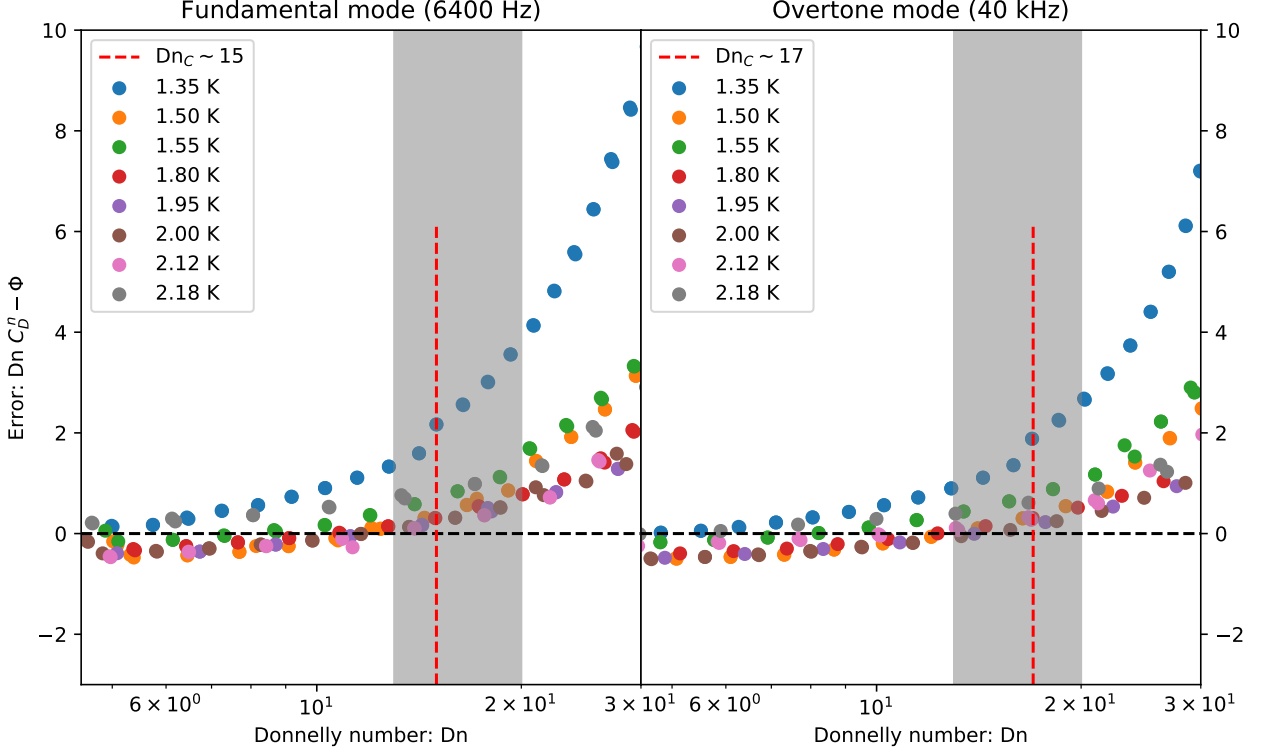


Figure 9: A zoomed plot of numerical errors from laminar regime fit $C_D^n \text{Dn} - \Phi$ with $\Phi = 4.9$ as a function of the Donnelly number Dn . Left image: Errors in fork's fundamental mode, Right image: Errors in fork's overtone mode, Black dashed lines: the normed laminar fit baselines, Grey areas: the possible critical values for Dn from the previous plot, Red dashed lines: The estimated values for critical Dn_C .

Our estimated value for critical Donnelly number Dn_C for temperature curves $T > 1.6$ K and for both oscillation modes is $\text{Dn}_C \sim 16$. The approximate shared value of critical Donnelly number proves the high-frequency regime validity and thus the possible domination of classical turbulence from normal component.

We note that it is interesting to find the laminar pre-factor $\Phi = 4.9$ to be same for both oscillation modes. The shared critical Dn_{crit} was expected from the dynamical similarity principle, but the shared Φ is a result of different principle - the fact that both modes have the same effective mass m_{eff} (see [?]).

1. Conclusions

In this chapter we generalize the analysed experimental and numerical results.

Experimental conclusions

We investigated systematic, high-Stokes flows of Helium-II at a range of temperatures $T \in \langle 1.3 \text{ K}, 2.18 \text{ K} \rangle$ generated due to several types of oscillators - vibrating wire, tuning fork and torsionally oscillating disc. All of them were kept in high-frequency regime (Stokes number $\text{St} \gg 1$).

Within the area of low peak velocities, the normal component is laminar and superfluid component remains potential (or stationary in case of torsional disc).

When we consider no remnant quantized vortices attached to the oscillator body, we can think in two independent velocity components, so the measured drags can be analysed separately as well. In this limit we treat the normal component as a classical viscous fluid, resulting naturally in inverse scaling of measured normal drag coefficient with the Donnelly number Dn : $C_D^n \propto \text{Dn}^{-1}$. Assuming that superfluid component doesn't contribute to the drag, the universal scaling holds until a critical velocity U_C for a given oscillator is achieved. Or, generalising it for all oscillator modes, until a critical dimensionless velocity $\hat{U}_C = U_C / \sqrt{\kappa \omega}$ is achieved.

In general, we recognize between four types of hydrodynamical states of Helium-II. We label the instabilities formed due to normal component as "CT" (classical turbulence) and due to superfluid component as "QT" (quantum turbulence):

- No CT nor QT present: laminar regime as described above, working universal scaling on normal component, superfluid component is potential or not moving at all, observed with all used oscillators ($\text{Dn} \lesssim 1$ for vibrating wire, $\text{Dn} \lesssim 5$ for oscillating disc and $\text{Dn} \lesssim 15$ for both oscillation modes of tuning fork).
- CT present without QT: normal component expected to origin a classical non-linear behaviour after reaching critical value of Donnelly number (thus universal scaling holds), superfluid component expected to remain potential, observed only with tuning fork at both oscillation modes for temperatures higher than $T > 1.6 \text{ K}$ with Donnelly number between $16 \lesssim \text{Dn} \lesssim 50$.
- QT present without CT: occurs if critical velocity given by Glaberson-Donnelly in-

stability (reconnection of remnant vortices) is achieved sooner than the critical Donnelly number, generally hard to prove such situation occurred since the CT use to appear almost immediately due to mutual friction. However, there is an indication that such phenomenon may happened in the case of torsionally oscillating disc at lower temperatures $T < 1.6$ K.

- Both CT and QT present: both normal and superfluid components expected to contribute to the drag, occurs when both critical velocity U_{crit} and Donnelly number Dn_{crit} are achieved, observed with all used oscillators.

To summarize, Glaberson-Donnelly instability (QT) occurs upon reaching a critical dimensionless velocity \hat{U}_C , while the instability in the normal component is governed upon reaching a critical Donnelly number Dn_C . All of the phase states were observed during experiments on oscillating bodies as descibed in previous chapters.

The last plot we show in **Figure (1.1)** from the hydrodynamical regime, is the *flow phase diagram*, summarizing all measured oscillators and their critical Donnelly numbers and critical dimensionless velocities. We also marked our estimated areas, where the transitions to non-linear regimes emerge.

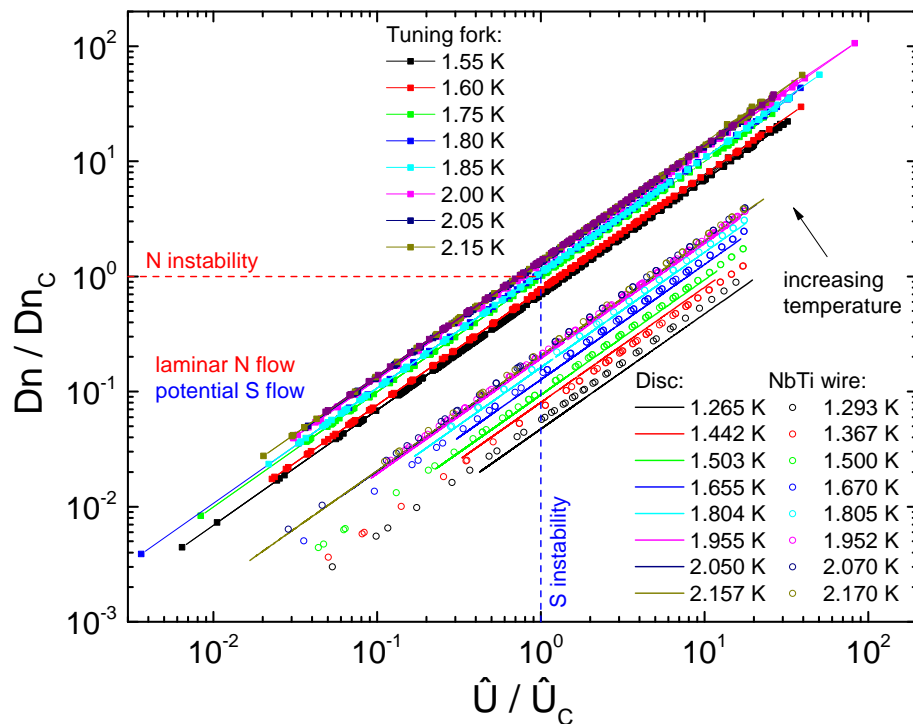


Figure 1.1: Plot of scaled critical Donnelly numbers and critical dimensionless velocities for for all used oscillators. Dashed lines marks the areas of transition from laminar/potential regimes to the non-linear ones, both for normal and superfluid component.

Ballistic regime

In this section, we demonstrate the limits of universal scaling validity. In **Figure 1.2** we plot the scaling function of Weissenberg number $f(Wi) = f(\omega\tau)$, as introduced in (??), together with the experimental results obtained using a tuning fork in two-fluid regime (presented in previous chapter) and in ballistic regime ($T < 0.6$ K). These regimes represent the Newtonian hydrodynamics ($Wi \ll 1$), governed by Navier-Stokes equations, and a non-newtonian gas dynamics.

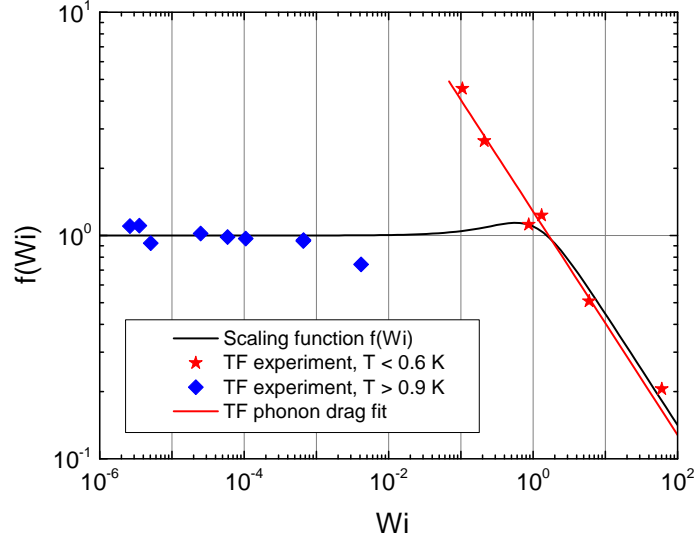


Figure 1.2: Plot of scaling function $f(Wi)$ as proposed in (??) compared with the experimental results of tuning fork in both low and ultra-low temperatures.

Black line: fit of the scaling function, Red line: fit to the phonon drag [?], Blue dots: experimental data collected from mentioned experiments, Red dots: experimental data collected from ultra-low temperature range. In all experiments we used the same tuning fork on both oscillation modes.

Both asymptotics for $Wi \rightarrow 0$ and $Wi \rightarrow \infty$ are identical in the means of quasi-classical description of the excitation gas. The mean free paths (or relaxation times) therefore can be calculated quantum-mechanically. The derived behaviour of scaling function ($f(Wi) \sim 1$ for $Wi \ll 1$ and $f(Wi) \propto 1/\sqrt{Wi}$ for $Wi \gg 1$) reflects the experimental data, except for the transitional area $Wi \sim 0.1$, where a peak emerged. However, this is the range where the fluid reaches a non-ballistic regime $Kn \sim 1$ earlier, than the non-Newtonian one ($wi \sim 1$). Hence, the assumptions of scaling function derivations are no more valid and thus our prediction $f(Wi) \propto 1/\sqrt{Wi}$ does not hold.

Simulation conclusions

We proposed an effective numerical method to compute the time evolution of vortex ring in superfluid He-II. All numerics is implemented in Python 3 and publicly uploaded on GitHub repository.

Performance of vortex filament model was improved by neglecting the Biot-Savart integral, showing that the percentual errors are small, and updating the LIA calculation instead. Simulation well replicates the physical processes and performs sufficient stability when using testing vortex ring of radius $R \in \langle 500, 2000 \rangle \mu\text{m}$ in resolution $\delta \in (60 - 100) \mu\text{m}$.